

## A LOG- $\omega$ TURBULENCE MODEL FORMULATION FOR FLUTTER ANALYSIS WITH HARMONIC BALANCE

Michael Müller, Hans-Peter Kersken, Christian Frey

Institute of Propulsion Technology  
German Aerospace Center (DLR)  
Linder Höhe

51147 Cologne, Germany

mi.mueller@dlr.de, hans-peter.kersken@dlr.de, christian.frey@dlr.de

### ABSTRACT

*When considering flutter problems, unsteady effects in turbulence quantities are frequently not taken into account when using time-linearized methods. However, several studies have demonstrated that it can be necessary to resolve those effects in certain cases. The harmonic balance method is inherently able to capture the time dependent behaviour of the turbulence model. However, the method can suffer from instabilities due to problems in the turbulence model. As a possible solution, a logarithmic formulation of the  $\omega$  equation of the Wilcox  $k$ - $\omega$  model is applied to the Harmonic Balance method in this paper. The combination is validated using a flutter computation of the NACA 3506 airfoil. One of the operating points exhibits significant oscillations in a shock induced separation. Resolving the unsteady behaviour of the boundary layer proved to be crucial to obtain a converged solution with the harmonic balance method. Both model variants were able to achieve satisfactory results. However, the  $\log(\omega)$  model variant was able to provide advantages in accuracy and convergence, especially under unfavourable conditions.*

### INTRODUCTION

Time-linearized methods are frequently used to assess the aeroelastic behaviour of turbomachinery blades and vanes. In those methods, the unsteady effects on the flow field are taken into account by linearizing the flow equations and considering a harmonic perturbation of the steady state solution. Sometimes, it is assumed that turbulence models do not need to react to

the oscillations in the flow to capture the aeroelastic behaviour with sufficient accuracy. Therefore, the steady state solution of the turbulence model is never updated. This method usually performs well when considering phenomena like flutter oscillations for the most common flow and operating conditions [1]. However, as e.g. Rendu et al. [2] showed, resolving the unsteady oscillations of the turbulence model can be necessary for some cases. This ensures not only an accurate prediction the damping coefficients, but in some cases it is required to get any converged solution at all. Utilizing common time-linearized methods to capture those effects is not necessarily straight-forward, e.g. Philit et al. [3] linearized the  $k$ - $\omega$  turbulence model for this purpose. A different approach is to use the common turbulence models in a solution method that is inherently able to capture the oscillations in the turbulent quantities. One example is the non-linear frequency domain method harmonic balance. While Heners et al. [4] demonstrated that the method is able to accurately predict the damping coefficients for a case with a shock wave boundary layer interaction, the method sometimes lacks stability [5]. This problem is not limited to flutter cases. Harmonic balance can also be used to efficiently investigate forced response or general multi row cases. A sufficiently accurate and stable turbulence model is necessary to provide all capabilities of standard URANS solvers. The insufficient stability, caused by unphysical oscillations in the turbulent quantities, can be addressed by reformulating the turbulence model to use a logarithmic  $\omega$  equation. In this paper, the different formulations are compared using a flutter case with different flow conditions. One operating remains sub-

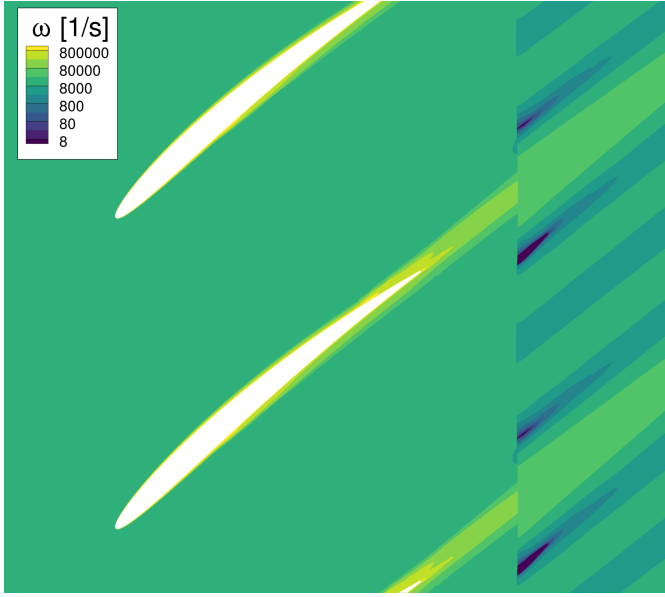


**FIGURE 1:** Oscillations in  $\omega$  around a poorly resolved wake in a rotating duct segment

sonic and provides a baseline comparison. The second operating point shows an oscillating shock induced separation which causes a significant time dependent behaviour in the boundary layer. The flow conditions for this point are similar to the cases examined by Duquesne et al. [6] and Heners et al. [4].

## NUMERICAL METHOD

In contrast to the flow quantities like density or pressure, the value range of the variables used in the common two equation turbulence models regularly spans several orders of magnitude. Especially the turbulent dissipation rate  $\omega$  used in models like Wilcox  $k-\omega$  [7] or Menter's SST  $k-\omega$  [8] model changes rapidly from low free stream values to very high values close to the wall, in separation bubbles or in wakes. In the harmonic balance method, the temporal evolution of  $\omega$  is approximated by a finite Fourier series. High gradients in this signal can lead to oscillations resembling the Gibbs phenomenon. Due the high peaks combined with small average values, the reconstructed  $\omega$  at the sampling points can reach unphysical negative values. This behaviour is visible in figure 1 where a wake with high values of  $\omega$  passes from a stator into an empty rotating duct segment. Here, this wake must then be represented by three harmonics as an unsteady phenomenon in the rotating duct. However, the high but narrow peak of the wake can not be correctly resolved and oscillations become visible. In this case  $\omega$  does reach values below zero, but this is not enough to strongly disturb the solver.

Negative values of  $\omega$  are unphysical and can cause stability problems. Limiting  $\omega$  to values greater than zero is not sufficient to ensure stability and accuracy. This decouples

the residuum calculated based on  $\omega$  from the actual value described by the harmonics, which has a negative impact on convergence. Increasing the number of harmonics considered also increases the computational cost. To address this problem, we implemented a logarithmic  $\omega$  formulation for turbulence models based on the work of Bassi et al. [9]. There, the reformulated turbulence model was used to deal with oscillations in a RANS discontinuous Galerkin solver. A logarithmic formulation of the  $\omega$  equation can offer two advantages. Firstly, the inverse function  $e^{\log \omega}$  always returns a positive value. Secondly, the value range of the new variable  $\log \omega$  is smaller than that of  $\omega$ . This also means that the gradients, for instance between the peak in the wake and the surrounding freestream values of  $\omega$ , get smaller. The two turbulence model formulations remain mathematically equivalent, but differences may occur due to discretization.

The derivation is straightforward by starting e.g. from Wilcox's  $k-\omega$  equations [7]:

$$\frac{\partial}{\partial t}(\rho k) + \frac{\partial}{\partial x_j}(\rho u_j k) = P_k - \beta_k \rho \omega k + \frac{\partial}{\partial x_j} \left[ (\mu + \sigma_k \mu_T) \frac{\partial k}{\partial x_j} \right] \quad (1)$$

$$\frac{\partial}{\partial t}(\rho \omega) + \frac{\partial}{\partial x_j}(\rho u_j \omega) = \alpha \frac{\omega}{k} P_k - \beta_\omega \rho \omega^2 + \frac{\partial}{\partial x_j} \left[ (\mu + \sigma_\omega \mu_T) \frac{\partial \omega}{\partial x_j} \right] \quad (2)$$

with the turbulent kinetic energy  $k$ , the specific dissipation rate  $\omega$ , and the production term  $P_k$ . A variable  $\tilde{\omega}$  can be introduced

$$\tilde{\omega} = \log \omega \iff \omega = e^{\tilde{\omega}} \quad (3)$$

The new variable  $\tilde{\omega}$  can now be substituted in for  $\omega$  in Eqn. (1) and Eqn. (2). This substitution is only meaningful if  $\omega$  is a dimensionless quantity, therefore the following equations are to be understood as dimensionless. The result can be simplified to Eqn. (4) and Eqn. (5):

$$\frac{\partial}{\partial t}(\rho k) + \frac{\partial}{\partial x_j}(\rho u_j k) = P_k - \text{Re} \beta_k \rho k e^{\tilde{\omega}} + \frac{1}{\text{Re}} \frac{\partial}{\partial x_j} \left[ (\mu + \sigma_k \mu_T) \frac{\partial k}{\partial x_j} \right] \quad (4)$$

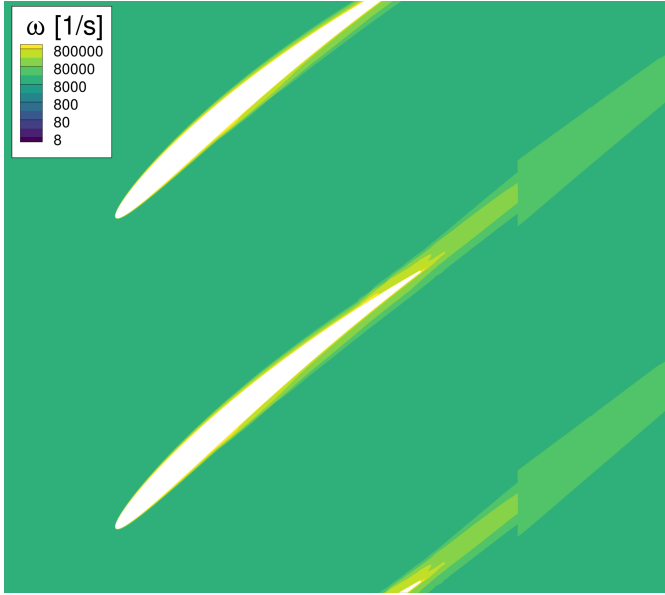


**FIGURE 2:** Reduced oscillations in  $\omega$  when calculated from the solution obtained with the logarithmic formulation

$$\frac{\partial \rho \tilde{\omega}}{\partial t} + \frac{\partial \rho u_j \tilde{\omega}}{\partial x_j} = \frac{\alpha P_k}{k} - \text{Re} \beta_\omega \rho e^{\tilde{\omega}} + \frac{1}{\text{Re}} \frac{\partial}{\partial x_j} \left[ (\mu + \sigma_\omega \mu_T) \frac{\partial \tilde{\omega}}{\partial x_j} \right] + \frac{1}{\text{Re}} (\mu + \sigma_\omega \mu_T) \left( \frac{\partial \tilde{\omega}}{\partial x_j} \right)^2 \quad (5)$$

This variable substitution adds an additional term in Eqn. (5) compared to its origin, Eqn. (2). The effect of the logarithmic reformulation is visible in Fig. 2. As in Fig. 1, the wake has to be resolved in the rotating duct segment by three harmonics. Oscillations are still visible, however their magnitude is significantly reduced. In particular there are no longer values below zero which can prove problematic for the stability and accuracy of the simulation. Figure 3 compares the incoming wake profile to the profiles resolved in the rotating reference frame. The wake profile of the  $k$ - $\omega$  simulation is plotted in blue, the corresponding result of the Fourier decomposition and reconstruction done in the harmonic balance solver is plotted in black. The unphysical oscillations are clearly visible, one undershoot reaches values below 0. In contrast,  $k$ - $\log(\omega)$  does not exhibit the strong undershoots with a comparable inflow profile. Additionally, the peak value is better represented and the wake is now resolved slightly sharper.

The reformulated models are also compatible to commonly used modifications, e.g. those used to ensure realizability and improve the prediction of the production of  $k$  in stagnation points or shocks. The modification proposed by Kato and Launder [10] is used in the simulations presented here. Using the substitution of Eqn. (3) it is also possible to use other

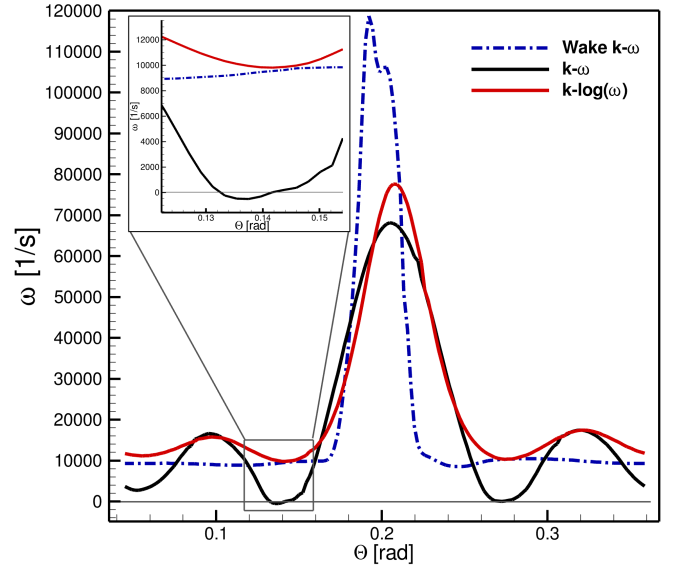


**FIGURE 3:** Reconstructed  $\omega$  in the rotating channel. The wake profile transported into the interface is coloured blue. The resulting profiles in the first cell of the rotating reference frame is plotted black for  $k$ - $\omega$  and red for  $\log(\omega)$

modifications, such as Durbin's constraint [11].

This reformulation of the  $k$ - $\omega$  and the SST model has been implemented in DLR's turbomachinery CFD solver TRACE [12]. TRACE uses the finite volume approach to solve the Reynolds-averaged Navier-Stokes (RANS) equations. The density based, compressible solver attains second order accuracy using Roe's upwind scheme and a MUSCL extrapolation. A van Albada type flux limiter is used to smooth large gradients, e.g. in the vicinity of shocks. For the solution of turbulence equations a conservative, segregated method is used. A second order Euler backwards method is used for time domain URANS simulations. The reformulated models were validated on basic turbulence modelling cases in [13]. As expected for mathematically identical models, the grid converged solutions remained identical between the two model formulations.

The Harmonic Balance solver implemented in TRACE is build upon the RANS/URANS solver. The aim of the method is to solve the RANS equations for time periodic solutions in the frequency domain. The RANS equations can be written as

$$\frac{dq(x,t)}{dt} + R(q(x,t)) = 0 \quad (6)$$

with the vector of conservative variables  $q$ , the discretised residual vector  $R$  and the physical time  $t$ . For a time periodic flow field,  $q$  can also be expressed as a partial Fourier series. Equation 6 can then be formulated in the frequency domain:

$$ikw\hat{q}_k + \widehat{R(q)}_k = 0 \quad (7)$$

where  $\hat{q}_k$  are complex valued Fourier coefficients for the conservative flow variables. The residual  $\widehat{R(q)}_k$  is now also complex. As a partial Fourier series, only a finite number of harmonics,  $k = 0, \dots, K$ , are considered. Due to the inherent non-linearity of the Navier-Stokes equations  $\widehat{R(q)}_k$  may depend on the flow variables  $\hat{q}_k$  of all harmonics. Several methods with varying degrees of complexity and accuracy have been developed to solve Eqn. (7) by giving different expressions for  $\widehat{R(q)}_k$ . The simplest is to linearise the equation with the intention of completely decoupling the different harmonics from each other [14]. In a related approach, nonlinear correction terms are added to model the nonlinearity [15, 16]. In the HB method the nonlinear residuals are computed in a different manner [17]. They are first calculated in the time domain and then transformed into the frequency domain via a discrete Fourier transformation (DFT).

$$\widehat{R(q)}_k = \mathcal{F}(R(\mathcal{F}^{-1}\hat{q})) \quad (8)$$

with Eqn. (7) this leads to base equation for the harmonic balance method:

$$ikw\hat{q}_k + \mathcal{F}(R(\mathcal{F}^{-1}\hat{q})) = 0 \quad (9)$$

with  $\mathcal{F}$  the DFT and  $\mathcal{F}^{-1}$  its inverse. Before the residual in the frequency domain can be calculated, an inverse DFT reconstructs several solutions for different points in time from the Fourier coefficients  $q_k$ . Once the residuals are calculated, the  $K + 1$  equations given in Eqn. (7) are solved by a pseudo-time-stepping scheme. The changes made to the turbulence models only affect the time domain calculation of the original residual function  $R(q)$ . More details about the Harmonic Balance solver implemented in TRACE can be found in [18].

## TEST CASE

The  $k\text{-log}(\omega)$  model is applied here to a compressor test case using the NACA 3506 profile, representing a section of a rotor with 20 blades. A rounded trailing edge is constructed by replacing the trailing edge region with a circle at 97% of the camber line, so that it tangentially intersects the suction and pressure side. An AVDR was applied starting from the leading edge and increasing to 1.05 at the trailing edge. This was done by linearly reducing channel height. The geometric definition of the test case can be found in Tab. 1:

Variable	Value
Airfoil	NACA 3506
Chord Length (Base Profile)	80 mm
Center of trailing edge circle	97% on camber line
Stagger Angle	40°
AVDR	1.05
Axial Position Leading Edge	51.6 mm
Domain length	160 mm
Number of blades	20
Hub Radius	195 mm
Base Channel Height	3 mm

This geometry was meshed with a structured grid. The first cell distance was chosen so that  $y^+ < 1$  and the stretching ratio at the blade surface was set to remain at or below 1.1. Additionally to this baseline grid with about 62.000 cells four more grids were created. Two of those keep the  $y^+$  constant, the other two also refine the first cell. All grids were created by increasing or decreasing the number of grid points by a constant value in both directions. The grids are labelled according to the number of cells compared to the baseline grid. Cell counts and approximate  $y^+$  values can be found in Tab. 2:

Name	Cell count	$y^+$
Grid 0.5 const. $y^+$	30,500	$y^+ \approx 0.5$
Grid 1 (baseline)	62,000	$y^+ \approx 0.5$
Grid 2 const. $y^+$	125,000	$y^+ \approx 0.5$
Grid 4 ref. $y^+$	304,000	$y^+ \approx 0.22$
Grid 16 ref. $y^+$	1,120,000	$y^+ \approx 0.07$

Two different operating conditions are considered. Operating point one (OP1) remains subsonic with a pressure at the outlet of 220 kPa and does not exhibit a strong dependence on the turbulence model. Operating point two (OP2) is transonic with a pressure of 205.5 kPa. The aerodynamic parameters and boundary conditions are summarized in Tab. 3 and 4.

Variable	OP 1	OP 2
Reynolds Number	$2.5 \cdot 10^6$	$3 \cdot 10^6$
Mach Number	0.58	0.74
Outlet static pressure	240 kPa	205.5 kPa
Inflow Angle	45°	45°

Variable	Value
Stagnation Pressure	293 kPa
Stagnation Temperature	293 K
Inflow Angle	45°
Turbulence Intensity	2%
Turbulence Length Scale	4.5e-5 m

The steady flow field for the second operating point is visualized in Fig. 4. To demonstrate the effect of the logarithmic model, the OP 2 test case was modified to include a rotating duct into which the wake of the airfoil is transported. The result for the  $k-\omega$  model is shown in figure 1. A translational movement normal to the chord, representing a bending mode, with a frequency of 227 Hz and an amplitude of 1.25 % of the chord length was added to both OP for the flutter simulations. This results in a reduced frequency of  $k = 0.667$  based on Eqn. (10). With this flutter movement, OP 2 displays flow phenomena similar to those examined by Duquesne et al. [6] and Heners et al [4]. In this case, the shock interacts strongly with the boundary layer, making the correct treatment of turbulence important.

$$k = \frac{2\pi fc}{u} \quad (10)$$

The harmonic balance method with three harmonics was used to calculate aerodynamic damping curves for both versions of the turbulence model. While a single harmonic is not yet sufficient for harmonic convergence, the damping curves calculated with three and six harmonics are identical for both model variants. For suitable inter blade phase angles (IBPA), multi passage time domain URANS simulations were also performed. A simulation was judged as converged when the variance in massflow, pressure ratio and the aerodynamic work on the blade dropped below 0.01%.

## RESULTS

The aerodynamic damping curve for the first operating point is plotted in Fig. 5. The unsteadiness in the boundary layer is minimal and the turbulence model has no large effect on the damping curve. As expected, the two model variants do not show relevant differences. This curve remains identical if the higher harmonics of the turbulence model are neglected.

The aerodynamic damping coefficients for the second operating point and both turbulence model variants are depicted in Fig. 6. Additionally, the results of time domain URANS simulations are marked for several IBPA. The time domain simulations agree very well with their respective frequency domain counterparts. The two model variants predict qualitatively the

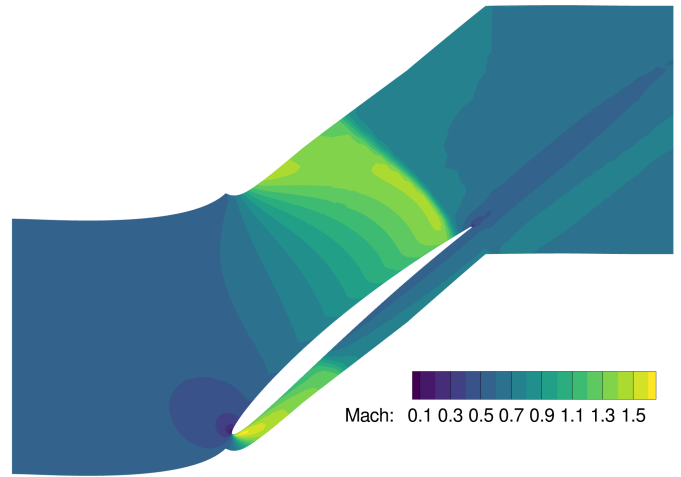


FIGURE 4: Mach number around the NACA 3506 airfoil

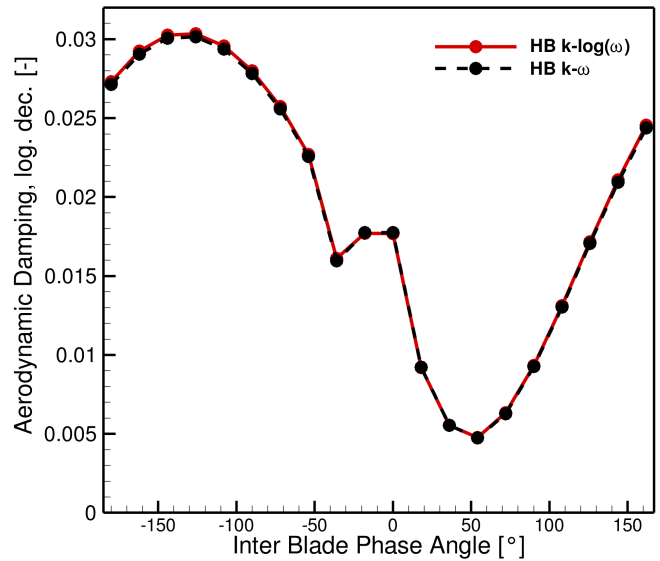
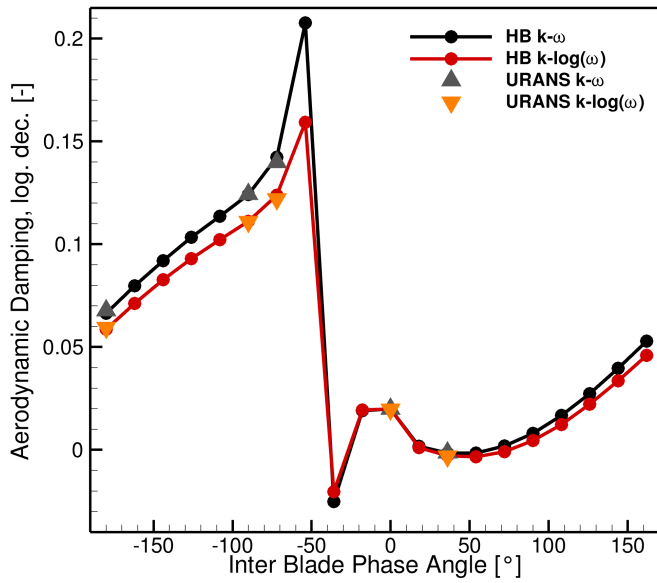


FIGURE 5: OP 1: Aerodynamic damping coefficients for both turbulence model formulations

same damping curve. However, differences are visible especially for negative IPBAs. Since the solution on the baseline mesh has not yet reached grid convergence, certain differences can be expected.

For the this operating point it is necessary to account for the unsteady effects of the shock wave boundary layer interaction on the turbulence model by considering higher harmonics. It was not possible to bring all points of the flutter curve to convergence when only a time-averaged turbulence model was used. The choice of turbulence model variant did not influence that. The time-averaged approach is not the same as completely freezing the turbulence model in place, as commonly done for linearized calculations. The turbulence quantities will be up-



**FIGURE 6:** OP 2: Aerodynamic damping coefficients for both turbulence model formulations compared to time domain URANS results

dated every iteration based on the changes in the time averaged solution. The reason why this is insufficient is visible in Fig. 7. The shear stress on the blade surface is plotted at two different points in time for the IBPA  $-72^\circ$  point in Fig. 7. The points were chosen to visualize the extrema during an oscillation. Similarly to what Duquesne et al [6] demonstrated, the turbulence model has to account for very different flow states during one period. In this case the shock triggers a separation on the suction side of the profile. This separation bubble is open during part of the oscillation, but remains closed for most of it. The time resolved shear stress in the suction side separation bubble is depicted in Fig. 8 at 92% of chord. The separation with negative shear stresses is only present during part of the cycle. This is accompanied by a cyclic increase and decrease of the boundary layer thickness. The turbulence model has to be able to resolve this time dependent behaviour to correctly represent the physics and allow the simulation to converge.

The imaginary part of the first pressure harmonic is plotted in Fig. 9, again for an IBPA of  $-72^\circ$ . The effect of the shock is clearly visible in the peaks on the suction and pressure side. Together they will dominate the aeroelastic behaviour. The peak on the pressure side is stronger and sharper compared to the suction side. The two model variants agree very well with each other at the pressure side peak. There is a slight difference in the peak location between the URANS and HB simulations of a single cell. However, the very good agreement of URANS and HB in Fig. 6 demonstrates that this does not significantly affect the aerodynamic damping. Contrary to the first shock, HB and URANS agree well on the pressure harmonic at the trailing edge shock position. Only here, in the region of the

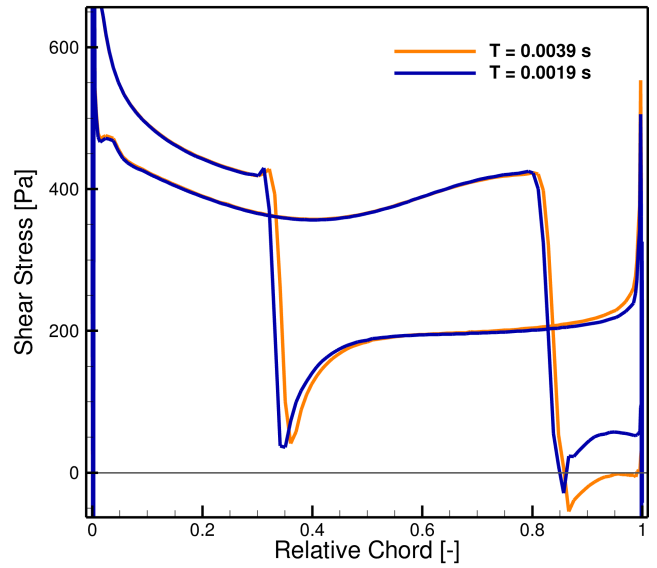


**FIGURE 7:** Extrema of the instantaneous shear stresses for HB  $k-\omega$  OP2 and an IBPA of  $-72^\circ$

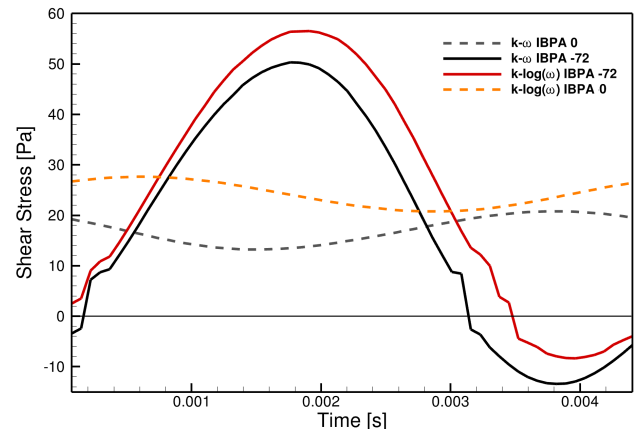


**FIGURE 8:** Time resolved shear stress at 92% of chord length for different IBPA

periodic flow detachment, are differences between the turbulence model variants visible. In contrast, where the two model variants coincide in the flutter curve, for IBPAs from  $0^\circ$  to ca.  $90^\circ$ , the flow reattaches after a small shock induced separation at the same position. This is visible in the time dependent shear stresses pictured in Fig. 8. Compared to an IBPA of  $-72^\circ$ , the shear stresses never reach negative values for an IBPA of  $0^\circ$  at this position. Since the flow is always attached, there are no strong time dependent changes in the turbulence quantities. The two model variants do not differ noticeably from each other under these conditions.

With increasing IBPAs, the flow starts to become unstable and differences due to the turbulence model emerge. This sensitivity of the test case to the turbulence model is not limited to

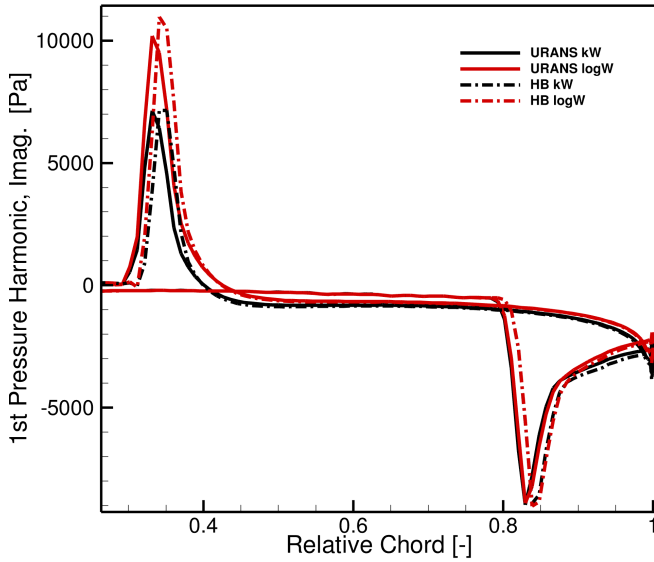


**FIGURE 9:** Imaginary part of the first pressure harmonic for HB OP2 and an IBPA of  $-72^\circ$

the pressure side shock. If the modification of the production of turbulent kinetic energy of Kato and Launder [10] is replaced by Durbin’s constraint [11], the other shock also induces a very small separation during part of the oscillation. The shape of the resulting flutter curve is almost unchanged, but again slightly shifted especially for negative IPBAs.

The pulsating separation bubble is visible in both turbulence model variants and qualitatively behaves in the same way. To investigate the differences visible in Fig. 6 and 9, a grid refinement was also done for this operating point using steady RANS simulations. In this case, steady simulations are sufficient to demonstrate the differences of the model variants on grids that have not reached grid convergence. The isentropic Mach numbers on the blade surface are plotted in Fig. 10. The different grid levels are marked according to their cell count compared to the baseline grid. All pictured grids keep the  $y^+$  constant under refinement. The standard  $k-\omega$  model is depicted in blue colours, the logarithmic variant in red. The position of the shock does not depend on the model variant. This is also true for the time averaged shock positions when unsteady effects are accounted for with URANS or HB. Small differences in the peak values are visible between the different grid resolutions, but those do not mark a relevant shift in the shock position. The increased streamwise resolution smooths the plots and enables a better localization of the shock in between the neighbouring cells of the coarser grids. Since this is the same for both model variants, this does not offer an explanation for the differences in the damping curve.

More relevant differences are visible in the shear stress pictured in Fig. 11. Depicted are the results calculated on the baseline grid and two refined grids for each model variant. The refined grids used here are the finest grids of each refinement

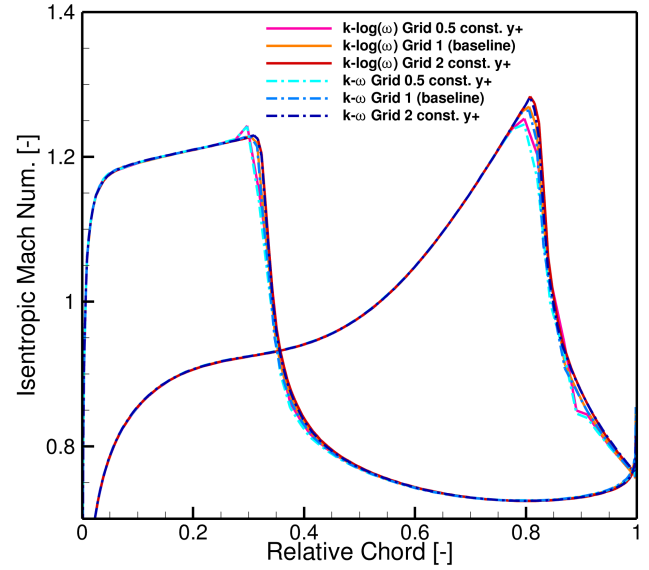


**FIGURE 10:** Isentropic Mach number around the blades for different grid resolutions with constant  $y^+$

method, one with a constant  $y^+$  and one with a refined  $y^+$ . For clarity, the solutions on grid 0.5 with constant  $y^+$  and grid 2 with refined  $y^+$  are not shown. Refining the baseline grid with a constant  $y^+$  results in a slight shift of the solution for the standard  $k-\omega$  variant. This is especially visible in the enlarged view, where the two dashed blue lines demonstrate this difference. The corresponding two orange lines for  $k-\log(\omega)$ , on the other hand, coincide for everything except the exact shock location, as previously discussed with Fig. 10. Nevertheless, a much larger difference in the shear stresses remain between the model variants than between the mesh resolutions. If, on the other hand, the first wall distance is also refined, the behaviour expected from the theory is obtained. Both model variants converge towards the same grid independent solution. The results on the finest grid are plotted in red for  $k-\log(\omega)$  and in black for  $k-\omega$  and can serve as a reference. Both of those solutions almost coincide and are in the vicinity of the two other  $\log(\omega)$  solutions in orange. The two  $k-\omega$  solutions in blue lie somewhat apart from all other results. Therefore, the mesh convergent result is very close to that of the  $\log(\omega)$  versions, even when calculated using the baseline grid. The jumps between the mesh resolutions tend to be larger for the standard  $\omega$  variant. Approaching grid convergence, however, requires a very good resolution of the boundary layer, with a  $y^+$  of less than 0.1. Basic turbulence model test cases already showed a improved behaviour of the logarithmic model variants under grid refinement [13].

The two model variants usually need a different number of iterations to reach convergence, as depicted in Fig. 12.  $k-\log(\omega)$  converges quicker for almost all IBPA, with few exceptions among those points that converge fastest anyway. For most points the speed-up is around 5-8%, with a maximum at

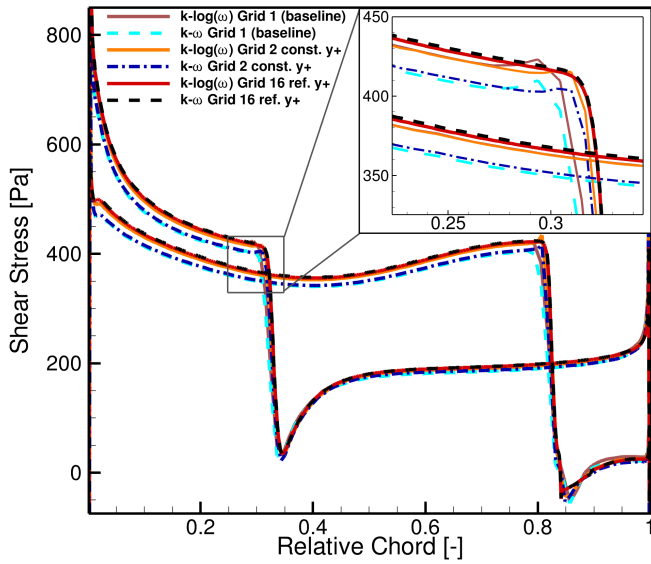


**FIGURE 11:** Shear stress on the blade surface for  $k-\omega$  and  $k-\log(\omega)$  models and different grid resolutions

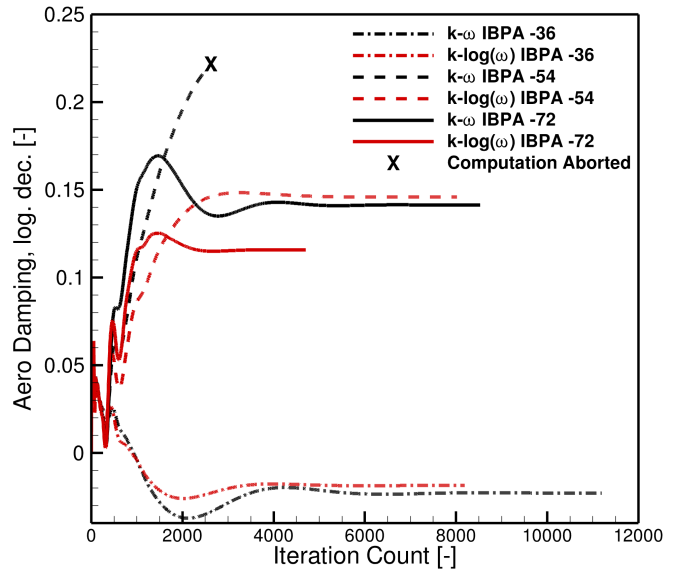


**FIGURE 13:** Convergence of the aerodynamic damping for several IBPA under unfavourable conditions

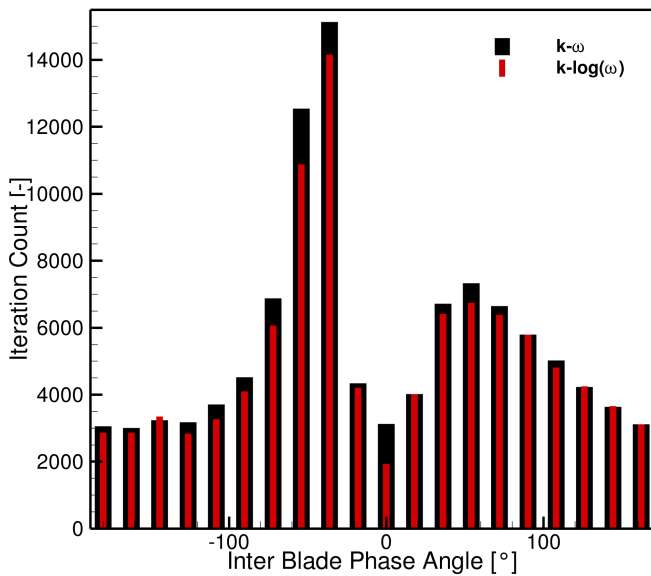


**FIGURE 12:** Number of iterations needed to satisfy the convergence criteria in OP 2

13% for an IBPA of  $-52^\circ$ . This speed-up is noticeable for the longer running simulations, which also determine the run time for a complete damping curve.

It is possible to demonstrate the instability problems with the standard  $k-\omega$  model by changing the turbulence quantities in the inflow and increasing the CFL number. An increase in the free stream  $\omega$  caused by a moderate change of the turbulent length scale from  $4.5 \cdot 10^{-5}$  m to  $2 \cdot 10^{-5}$  m is combined with an increased CFL number of 50. Otherwise the test case

is identical to OP 2. This causes a higher  $\omega$  in the detached flow region and in the wake. Due to the periodic detachment and reattachment of the flow, the wake has to be resolved by higher harmonics. The increased values of  $\omega$  in the boundary layer are transported into the wake, where the amplitude of the harmonics of  $\omega$  also increases. As visible in Fig. 13, this significantly influences the convergence of the affected IBPA. The negative IBPA from  $-36$  to  $-90$  are again affected most, as they show the strongest unsteady behaviour in the separation bubble. The  $k-\log(\omega)$  model can show its advantages under these condition and converges significantly faster. In the case of an IBPA of  $-54^\circ$  the  $k-\omega$  model reaches an unphysical flow state close to the trailing edge of the profile and the simulation terminates. The logarithmic model variant does not exhibit this problem and converges faster.

## SUMMARY AND CONCLUSIONS

A logarithmic formulation of the  $k-\omega$  turbulence model was implemented in DLR's turbomachinery CFD solver TRACE. This turbulence model variant was applied to two operating points of a flutter test case based on the NACA 3506 profile using the harmonic balance method. No differences between the model formulations were observed under the conditions of OPI. Including higher harmonics when solving the turbulence model did not affect the flutter curve or convergence, indicating that there are no relevant unsteady flow phenomena in the boundary layer. Both model variants performed equivalently with regard to accuracy and convergence.

The second operating point, however, was very sensitive to small changes in the turbulence model. The shock induced

separation on the suction side was heavily influenced by the oscillation of the shock for negative IBPA. Depending on the phase position in an oscillation, the separation bubble remained either detached for the last 15% of the cord or quickly reattached close to the shock. It was necessary to enable the turbulence model to resolve this unsteady behaviour of the boundary layer in order to get a converged solution. The two turbulence model variants did predict comparable aerodynamic damping curves, in excellent agreement with their respective time domain URANS simulations. However, differences were noticeable especially for those inter blade phase angles exhibiting the oscillating separation bubbles. Refining the grids with or without keeping  $y^+$  constant showed differences between the model variants, which agreed with the result of a previous study using only basic turbulence modelling test cases. The  $\log(\omega)$  model variant converges against the same grid independent solution as the standard  $k-\omega$  model. A substantial refinement of  $y^+$  is necessary to approach true grid independence, for both model variants. However, the  $k-\log(\omega)$  model generally showed smaller errors. For about half of the IBPAs, among them the longest running simulations, the logarithmic model converged in about 5% less iterations. For the rest, it performed largely on par with the standard variant.

The logarithmic model variants were implemented with the idea to bring more stability to harmonic balance simulations. In the case of the flutter problems considered in this paper, it compares favourably with the standard variants in terms of accuracy, grid dependence and convergence. In simple applications, such as the first OP, it did not bring any disadvantages. For simulations where the time dependent behaviour of the turbulence quantities has a large influence, however, we were able to demonstrate advantages of the  $k-\log(\omega)$  model. Under unfavourable conditions, this model was able to provide a converged solution where the standard model reached an unphysical flow state and terminated early. In our experience, the use of the logarithmic models can indeed help outside of academic test cases, if the stability problems are related to the turbulence model. However, determining this with certainty is difficult and time-consuming. In addition, the problems identified may not be easy to solve. The use of the  $\log(\omega)$  model variants could provide several advantages at minimal cost.

## NOMENCLATURE

### Abbreviations

AVDR	Axial velocity density ratio
CFD	Computational Fluid Dynamics
DFT	Discrete Fourier Transform
DLR	Deutsches Zentrum für Luft- und Raumfahrt (German Aerospace Center)
HB	Harmonic Balance
IBPA	Interblade Phase Angle
OP	Operating Point
URANS	Unsteady Reynolds Averaged Navier Stokes

### Latin

$i$	Complex unit
$k$	Turbulent Kinetic Energy
$K$	Turbulent Kinetic Energy
$Ma$	Mach number
$P$	Production of turbulent kinetic energy
$q$	Vector of conservative flow variables
$R$	Flow residual
$Re$	Reynolds number
$t$	Time
$u$	Velocity
$w$	Angular Frequency

### Greek

$\alpha, \beta$	Model constants of the Wilcox $k-\omega$ model
$\rho$	Density
$\mu$	Eddy viscosity
$\omega$	Turbulent dissipation rate

### Operators

$\mathcal{F}$	Fourier transform
$\mathcal{F}^{-1}$	Inverse Fourier transform

### Superscripts & Subscripts

$\hat{\cdot}$	Fourier coefficient
---------------	---------------------

## REFERENCES

- [1] Kersken, H.-P., Frey, C., Voigt, C., and Ashcroft, G., 2012. "Time-linearized and time-accurate 3D RANS methods for aeroelastic analysis in turbomachinery". *Journal of Turbomachinery*, **134**(5), p. 051024.
- [2] Rendu, Q., Philit, M., Labit, S., Chassaing, J., Rozenberg, Y., Aubert, S., and Ferrand, P., 2015. "Time-linearized and harmonic balance navier-stokes computations of a transonic flow over an oscillating bump". In 11th International Symposium on Unsteady Aerodynamics, Aeroacoustics & Aeroelasticity of Turbomachines.
- [3] Philit, M., Ferrand, P., Labit, S., Chassaing, J., Aubert, S., and Fransson, T., 2012. "Derivated turbulence model to predict harmonic loads in transonic separated flows over a bump". In 28th International Congress of Aeronautical Sciences.
- [4] Heners, J. P., Carraro, T., Frey, C., and Grüber, B., 2022. "Evaluating the aerodynamic damping at shock wave boundary layer interacting flow conditions with harmonic balance". *To be published in: Proceedings of ASME Turbo Expo 2022*. GT2022-81689.

- [5] Heeners, J. P., Vogt, D. M., Frey, C., and Ashcroft, G., 2019. “Investigation of the Impact of Unsteady Turbulence Effects on the Aeroelastic Analysis of a Low-Pressure Turbine Rotor Blade”. *Journal of Turbomachinery*, **141**(10), 09. 100801.
- [6] Duquesne, P., Rendu, Q., Aubert, S., and Ferrand, P., 2019. “Choke flutter instability sources tracking with linearized calculations”. *International Journal of Numerical Methods for Heat and Fluid Flow*, **30**, 01.
- [7] Wilcox, D. C., 2006. *Turbulence Modeling for CFD*, 3. ed. DCW Industries, La Cañada, USA.
- [8] Menter, F. R., 1994. “Two-equation eddy-viscosity turbulence models for engineering applications”. *AIAA J.*, **32**(8), Aug., pp. 1598–1605.
- [9] Bassi, F., Crivellini, A., Rebay, S., and Savini, M., 2005. “Discontinuous galerkin solution of the reynolds-averaged navier–stokes and  $k-\omega$  turbulence model equations”. *Computers & Fluids*, **34**, 05, pp. 507–540.
- [10] Kato, M., and Launder, B. E., 1993. “The modeling of turbulent flow around stationary and vibrating square cylinders”. In 9th Symposium on Turbulent Shear Flows, pp. 10.4.1–10.4.6.
- [11] Durbin, P., 1996. “On the k-3 stagnation point anomaly”. *Int. J. Heat Fluid Fl.*, **17**(1), pp. 89 – 90.
- [12] Becker, K., Heitkamp, K., and Kügeler, E., 2010. “Recent Progress In A Hybrid-Grid CFD Solver For Turbomachinery Flows”. In Proceedings Fifth European Conference on Computational Fluid Dynamics ECCOMAS CFD 2010.
- [13] Müller, M., and Morsbach, C., 2018. “A logarithmic w-equation formulation for turbulence models in harmonic balance solvers”. In ECCOMAS ECCM ECFD.
- [14] Hall, K. C., and Crawley, E. F., 1989. “Calculation of unsteady flows in turbomachinery using the linearized Euler equations”. *AIAA J.*, **27**(6), pp. 777–787.
- [15] He, L., and Ning, W., 1998. “Efficient Approach for Analysis of Unsteady Viscous Flows in Turbomachines”. *AIAA J.*, **36**(11), Nov., pp. 2005–2012.
- [16] Vasanthakumar, P., 2003. “Three dimensional frequency-domain solution method for unsteady turbomachinery flows”. PhD thesis, Durham University.
- [17] Hall, K. C., Thomas, J. P., and Clark, W. S., 2002. “Computation of Unsteady Nonlinear Flows in Cascades Using a Harmonic Balance Technique”. *AIAA J.*, **40**(5), May, pp. 879–886.
- [18] Frey, C., Ashcroft, G., Kersken, H.-P., and Voigt, C., 2014. “A harmonic balance technique for multistage turbomachinery applications”. In ASME Turbo Expo 2014: Turbine Technical Conference and Exposition, no. 45615, p. V02BT39A005.